

ExAOC error budget and performance predictions  
V1.0 July 22, 2004  
Bruce Macintosh LLNL

Sections flagged by a number sign # or in italics indicate a work-in-progress area in need of updating.

## 1.0 System performance goals:

The performance goals set out in the Gemini request for proposals are contrast<sup>1</sup> of  $10^7$  with an inner working distance of  $0.1''$ . Although the contrast goal might be achievable, it is highly unlikely that it can be achieved at  $0.1''$  radius (especially at longer wavelengths), and in any event the Gemini requirements are relatively arbitrary; our contrast goals should be set by the primary science goal – detection of a significant number of extrasolar planets – which leads to a requirement not just for high contrast but for significant scientific reach in terms of limiting target star magnitude.

Nonetheless, from previous simulations contrast  $10^7$  seems to be within the reach of ExAO and we will take it as a goal for moderate-brightness ( $m_I=5-7$ ) stars, with a second goal of good performance down to  $m_I=7-8$ . (See the science documents### for discussion of these requirements.) A detailed treatment of contrast vs angular radius and target star magnitude is beyond the scope of this initial document, and will come from more refined versions of the error budget and from simulations. This error budget is evaluated for a single field angle.

## 2.0 Assumed system parameters:

The following parameters were used to construct this error budget. Parameters highlighted in italics are preliminary values that need additional refinement.

### Telescope and atmosphere

Diameter	8.2 m
<i>r0 at 500 nm</i>	<i>0.2 m[1]</i>
Windspeed	20 m/s
<i>Residual telescope aberrations</i>	<i>20 nm[2]</i>

### Adaptive Optics System base parameters

Subaperture size	0.13 m
Update rate	2500 Hz
<i>3dB Bandwidth</i>	<i>150 Hz (Goal: 200 Hz)</i>

### Optical transmission (visible/IR)

Telescope	3 optics @ 0.96/0.98
AO common path	8 optics @ 0.96/0.98
Dichroic	1 optic @ 0.95/0.98
WFS optics	4 optics @ 0.99
Coronagraph optics	2 optics @ /0.98
Coronagraph stop	0.5 total transmission
Science camera	0.5 total transmission

---

<sup>1</sup> Note that we need to formally define contrast – this should be the subject of a future document.

Total WFS throughput	0.58
Total science throughput	0.19

**Optical errors (total; see Table 1 for breakdown by spatial frequency)**

<i>Total non-common-path errors</i>	20 nm[3]
<i>Residual calibration errors</i>	5 nm
<i>Common path errors</i>	10 nm
<i>Uncorrectable DM errors</i>	20 nm
<i>Post-coronagraph errors</i>	10 nm
<i>Power law for optical surface PSD</i>	-2.5
<i>Residual flexure</i>	10 nm

**Science channel parameters**

Science wavelength	1.65 microns
Filter bandwidth	0.3 microns
Detector QE	0.9
Zero magnitude point	26.3 (for 1 electron/second signal)

**WFS channel parameters**

Wavelength range	700-900 nm
Detector QE	0.6
Number of pixels per subap	4
Readnoise	7 electrons

**Target properties**

$m^1$	5
I-K	0.6
Science exposure time	3600 seconds
Parallactic rotation rate	0.2 degrees/second
Angular separation of interest	0.4 arcseconds

**Coronagraph parameters**

Residual diffraction	$5 \times 10^{-8}$
Throughput	50%
<i>Angular resolution loss</i>	0[4]

**Derived quantities**

WFS SNR	10.9
---------	------

[1] The atmosphere is modeled as a single ground layer except for the addition of a scintillation term from numerical modeling – see the scintillation report for details.

[2] Residual telescope aberrations after AO correction; note that as per Table 1 most of this is high-frequency. Detailed models of the Gemini mirrors are needed to evaluate this more correctly.

[3] NCP errors are assumed to be dominated by the WFS optics; errors in the science path would have more stringent requirements. These must be broken down further in future iterations.

[4] Many coronagraph will degrade the angular resolution / 80% EE radius; this effect has not been modeled.

### 3.0 Error budget and PSF components

Using the formalism in the appendix, we can produce an error budget for ExAOC that will allow us to not only predict Strehl ratio but also estimate final contrast at a given radius, as in Table 1. For each error source, in addition to its magnitude, a speckle lifetime and an estimated spatial frequency distribution has been used; some discussion of those distributions follow. Scattered light terms that do not scale directly from the magnitude of phase errors, such as coronagraph leakage and light scattered by amplitude errors, are also included in the table and will be discussed in more detail in a future document. In the following sections we will briefly discuss the properties of each error source and in several cases illustrate the PSF that would occur if that were the only error source; as discussed above, the final long-exposure PSF will be given by the sum of these separate PSFs, at radii where the diffraction component is negligible.

We divide each error source into three spatial frequency components: low frequencies (<4 cycles/pupil), corresponding to wavefront error sources that primarily scatter light beneath the occulting spot of the coronagraph; high frequencies (>30 cycles per pupil), which scatter light into the wings of the PSF at large angles; and the crucial mid-frequency range that corresponds to the dark hole in which we wish to detect planets. For each error source, we present the corresponding scattered-light intensity at a radius of 0.4 arcseconds, and the resulting speckle noise in a 3600-second exposure. (Note that since speckle noise occurs from the intensity of the PSF, which is already a squared quantity, the speckle noises add linearly rather than in quadrature.) The contribution to the final noise due to photon noise is also listed. The predicted detectable point source contrast –  $7.5 \times 10^{-7}$  at 0.4 arcseconds in a one-hour integration – agrees within a factor of two with more detailed simulations.



Figure 1 shows the contributions of each error source graphically. For comparison, **Error! Reference source not found.** shows a similar chart for a typical non-extreme AO system such as the current Keck AO. Note that we do not assume any PSF subtraction, either through observations of reference stars or through multi-wavelength imaging<sup>1,2</sup>; this is a conservative error budget for direct broadband imaging. If quasi-static PSF components can be removed through some post-

processing, requirements on static error sources could be relaxed. Key individual error sources are discussed in the following sections.

Scattered light source	low freq. WFE (nm)	mid freq. WFE (nm)	high freq. WFE (nm)	all freq WFE (nm)	Speckle lifetime (seconds)	PSF intensity 0.4 arcsec	PSF noise 0.4 arcsec 1 hour
Atmosphere		2.00	30.75		0.16	6.0E-08	7.7E-11
Telescope primary/secondary		0.50	20.00		1772.04	3.8E-09	5.0E-10
Telescope vibration	0.00	0.10	0.00	0.00	<b>1.00</b>	1.5E-10	4.8E-13
Initial calibration	5.00	1.00		5.00	1772.04	1.5E-08	2.0E-09
Atmospheric bandwidth	16.36	17.41	12.13	16.36	0.16	3.2E-06	4.0E-09
WFS measurement		40.17			0.01	2.4E-05	6.3E-09
Uncorrectable internal errors		0.00	23.00		1772.04	1.0E-20	1.3E-21
Quad cell changes	0.33	0.19	0.00	0.33	1772.04	5.7E-10	7.6E-11
<i>System Flexure</i>	<i>10.00</i>	<i>1.00</i>	<i>0.00</i>	<i>10.00</i>	<i>1772.04</i>	<i>1.5E-08</i>	<i>2.0E-09</i>
<i>Residual diffraction</i>						<i>5.00E-08</i>	
Post-coronagraph aberrations	8.21	4.86	3.00	8.21	1772.04	2.2E-08	2.9E-09
<i>Scintillation</i>					0.16	1.0E-06	1.3E-09
<i>Internal static intensity errs</i>						2.4E-08	3.1E-09
Photon noise							3.7E-09
<b>Total</b>	<b>19.81</b>	<b>43.85</b>	<b>44.96</b>	<b>65.86</b>		<b>2.9E-05</b>	<b>1.8E-08</b>

Table 1: ExAOC error budget for a one-hour observation. PSF intensity and PSF noise are normalized with respect to the peak intensity of the coronagraphic PSF, so that a PSF noise of  $1.5 \times 10^{-8}$  would represent a 5-sigma detection of a companion with a contrast relative to its primary of  $7.5 \times 10^{-7}$ .

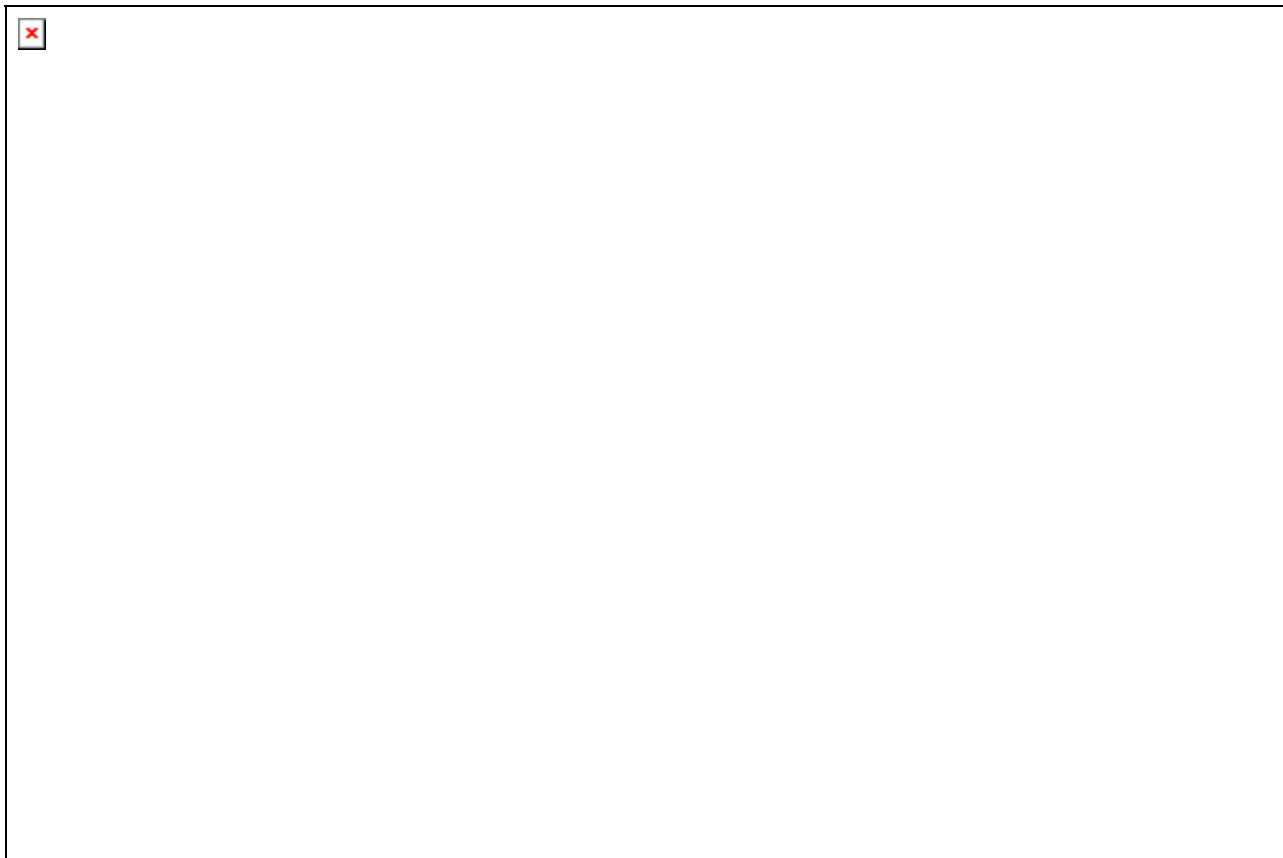


Figure 1: Contributions of each separate error source to the final PSF intensity (solid bars) and PSF noise (light bars) at 0.4 arcseconds separation in a one-hour exposure.

These error budgets have been constructed for a case with no PSF subtraction – ie, evaluating the contrast in a direct long-exposure image. The second revision of this document will present an error budget for a multiwavelength imager case, and integrated system analysis (most likely in the PDR phase) will explore PSF reference stars. ###

Quasi-static wavefront errors are currently treated with the most conservative assumption possible – that they do not decorrelate themselves but also cannot be subtracted via observations of reference stars. It is assumed that the instrument is used in a non-rotating mode, so that the telescope pupil remains fixed on the camera while the sky rotates; if derotated images are averaged together, this will result in a speckle lifetime equal to the time needed for one diffraction limit’s worth of rotation. This value (evaluated for a typical target near transit with a rotation rate of 0.2 degrees/minute) has been used for all quasi-static errors.

### 3.1 Atmospheric errors

Classic atmospheric fitting error – i.e., the portion of the atmospheric phase errors that cannot be corrected by the deformable mirror – is almost exclusively a high-frequency error source; a well-behaved DM can reproduce the band-limited components of almost any wavefront. This produces a PSF similar to the left portion of Figure 2, bright only outside the AO control region with a small amount of error close to the star caused by fourth-order terms in the PSF expansion. Of course, most AO systems do not produce PSFs of this shape, due to aliasing effects’ resulting in PSFs similar to the right portion of figure 7, where the dark hole is filled in. ExAOC will use a spatially-filtered wavefront sensor to block aliasing; at high Strehl ratios this can reduce the amount of mid-

frequency power by a factor of 100 or more<sup>#</sup>. This produces a significant increase in sensitivity, as speckles due to atmospheric fitting and aliasing errors are long-lived ( $t_{dec}=0.2-0.4$  seconds for a 10-m telescope).

In the current error budget, residual atmospheric error within the mid-frequency range has been set based on numerical simulations carried out by at LLNL by Lisa Poyneer; this term is nearly negligible in the error budget. The magnitude of the pure fitting error is calculated from the usual formulae for continuous DMs.

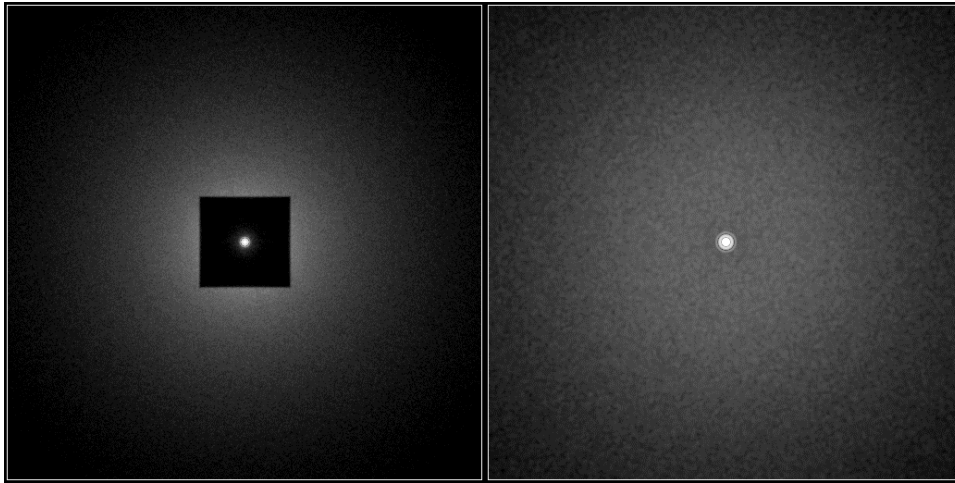


Figure 2: Simulated PSFs due to atmospheric fitting error (left) and fitting + aliasing errors (right.) Five second exposure monochromatic PSF with diffraction suppressed by pupil apodization.

### 3.2 Telescope static and vibration errors

Gemini telescope errors are currently only a rough estimate; their true magnitude will have to be determined through interactions with Gemini followed by AO system modeling, but there is no reason to expect the mid-frequency component to be large (except for the secondary mirror, which is expected to be replaced before ExAOC operation.) Residual errors due to the telescope are assumed to be essentially static, smoothing out only as the telescope pupil rotates with respect to the sky,  $\sim 1000$  seconds for small field angles at moderate elevations.

### 3.3 Initial calibration and residual static errors

The ExAOC optical design goal requires  $<25$  nm of non-common path optical errors between the wavefront sensor and the coronagraph input – challenging but not impossible. However, even this small amount would completely dominate final contrast sensitivity if not removed through calibration. Figure 3 illustrates the effect of small wavefront errors on final contrast.

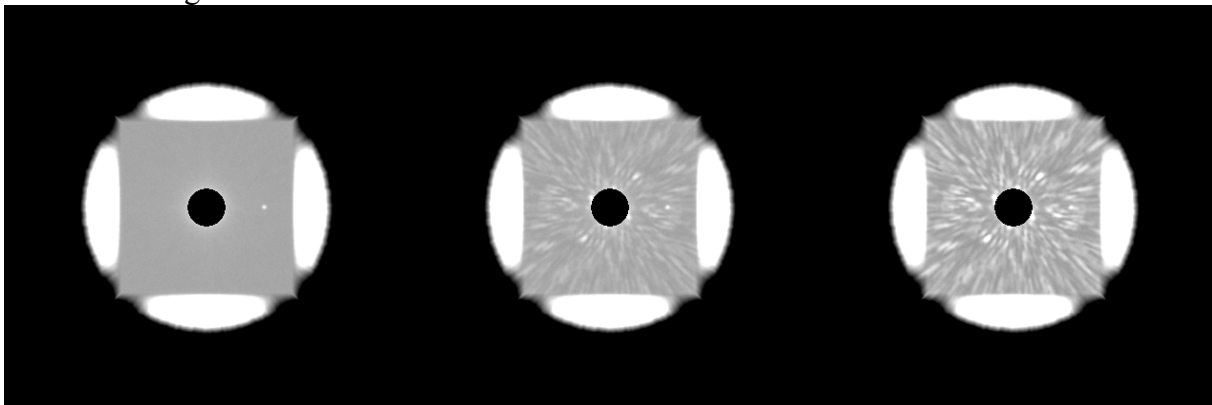


Figure 3: Three simulated 15 minute ExAO images similar to **Error! Reference source not found.**, with 0 (left), 2, and 4 nm RMS random static wavefront error (uniformly distributed in spatial frequencies out to the AO cutoff). This simulation was carried out with low winds (<5 m/s) to reduce the effect of atmospheric bandwidth errors.

Even if PSF subtraction is not used, appropriate observing modes can smooth out some of these speckles; in particular, if the system image rotator is operated to keep the telescope pupil fixed on the AO system rather than keeping the sky fixed, short-exposure images can be derotated and combined to cause both errors from the telescope and the AO bench to smooth out.

Achieving these error levels will be extremely challenging, but they are an order of magnitude less than those required for e.g. the Terrestrial Planet Finder mission. A companion paper discusses our approach to achieving and maintaining calibration, and we have demonstrated <2 nm RMS wavefront error with both a flat mirror and a 1024-actuator MEMS deformable mirror on a simple ExAO testbed, with corresponding contrast >10<sup>7</sup>. These errors are currently assumed to have a flat power spectrum inside the mid frequency range.

### 3.4 Atmospheric temporal bandwidth errors

One of the two main sources of scattered light within the dark hole is the finite temporal bandwidth of the AO system – its inability to keep up with the moving and evolving atmospheric turbulence. Figure 4 shows the corresponding PSF – for a single Taylor screen, this has a characteristic “butterfly” shape, though of course multiple layers and deviations from frozen-flow will cause the PSF to become more symmetric. In this is the main source of scattered light close to the star. As with other atmospheric errors, this produces moderately long-lived (0.2-0.4 second) speckles, so that even with ExAOC’s aggressive 2500 Hz sample rate, this remains the dominant external term in the final contrast budget. The Altair-style self-optimizing controller may help reduce these errors. The spatial frequency distribution of these errors is currently set by a lookup table based on simple pure-delay simulations carried out by Macintosh; analytic formulae from Rigaut et al (REF) give similar results.

### 3.5 Wavefront sensor measurement noise

The second major source of scattered light inside the AO control radius is wavefront errors injected by the AO system itself due to finite SNR in the wavefront sensor. By definition, this is a source only of errors within the controlled range of spatial frequencies, and can be significant for dim target stars. Fortunately, since these errors are uncorrelated from measurement to measurement, they produce speckles that decorrelate rapidly – compare the smoothness of the right-hand image in Figure 4 to the left-hand image. In a closed-loop controller this decorrelation does not take place at the full update rate of the AO system; we have assumed a  $t_{dec}=1/f_b$  where  $f_b$  is the 3db bandwidth of the controller, but detailed closed-loop AO simulations will be needed to determine the exact evolution of the speckle pattern. The spatial distribution of these errors is assumed to be flat within the mid frequency range. This is known to be an oversimplification; the true spatial distribution depends on the details of the reconstructor (and to a lesser extent the DM.) The flat distribution will be replaced with a lookup table from numerical modeling of the AO controller. However, the Fourier modal gain optimization appears to act to flatten the spatial power spectrum of the readout noise, so flat-spectrum model may not be a bad approximation.

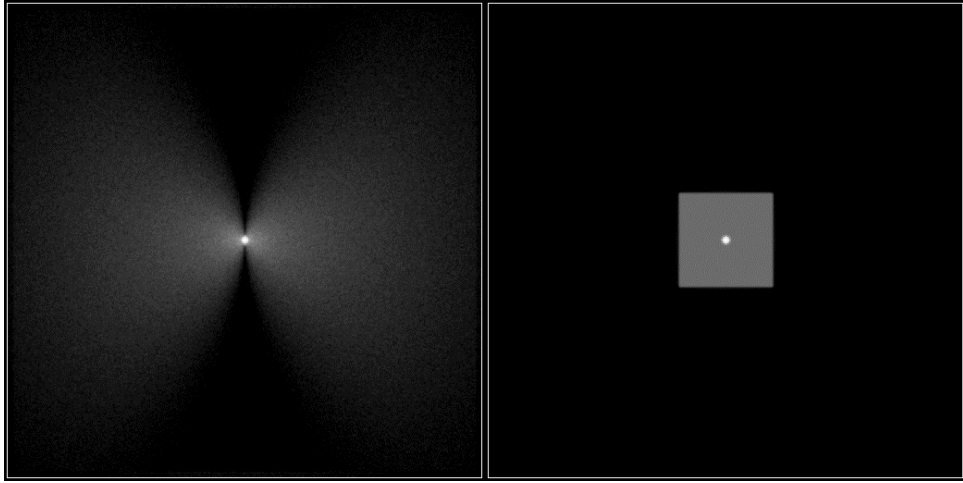


Figure 4: Left: Simulated PSF due to temporal bandwidth errors with the wind moving left to right. Right: Simulated PSF due to wavefront measurement noise for a spatially-filtered direct-phase measurement wavefront sensor. Five second exposure monochromatic PSF with diffraction suppressed by pupil apodization.

### 3.6 Quad cell gain changes

Many AO systems, including ExAOC, use Shack-Hartmann wavefront sensors in a quad cell mode with only 2x2 pixels per subaperture. Although this is the most efficient in terms of detector real estate and readout noise, it results in a sensor whose gain is a function of the size of the Shack-Hartmann spot. The spot size, of course, can change due to changes in  $r_0$  or even random realizations of the wavefront error across a subaperture at a given  $r_0$ . These changes in gain can have two detrimental effects. First, imperfect knowledge of the gain can lead to decreased bandwidth in the AO system. Second, and more significantly, if the AO system is attempting to maintain a non-flat residual wavefront offset from flat on the wavefront sensor, e.g. due to non-common-path errors, the mis-estimation of the gain will cause the average centroids to be offset from the desired wavefront, over- or under-correcting the non-common-path errors. Several techniques have been suggested to overcome this, including the modulation of the wavefront by the AO system with a known error signal at a rate beyond the AO control bandwidth<sup>3</sup>, but it is unclear if these are precise enough for our error budget requirements.

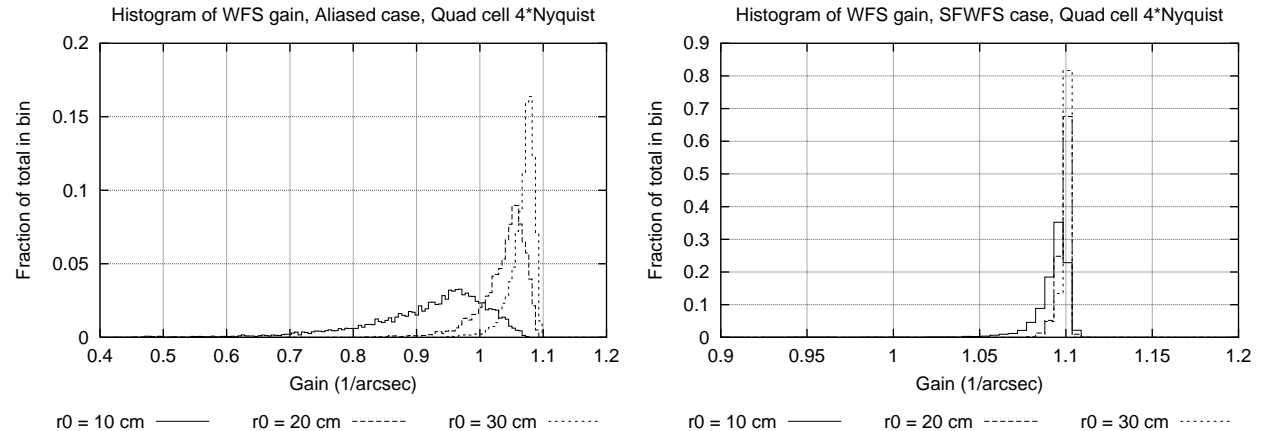


Figure 5: Histogram of quad-cell gains for Shack-Hartmann wavefront sensors,  $d=16$  cm, with (left) and without (right) a spatial filter. Note the change in axis scales.

Fortunately, an additional advantage of the ExAOC spatially-filtered wavefront sensor is that it acts to suppress these changes in gain. Figure 5 shows histograms of the gain at three different  $r_0$  values for a conventional and spatially-filtered WFS. The SFWFS values show extremely little scatter or  $r_0$

dependence, nearly matching the values for a perfect diffraction-limited subaperture. This is of course due to the removal of high spatial-frequency wavefront errors; this ensures that the wavefront across a given subaperture consists primarily of tip and tilt components. As a result, the WFS gain can be predicted with considerable accuracy even without an estimate of  $r_0$ .

#### **4.7 Post-coronagraph errors**

Errors after the coronagraph occulting spot are often neglected in ExAO modeling, since the coronagraph spot blocks a significant fraction of the light of the star. These can still be significant; to first order, the light scattered after the coronagraph is given by the light scattered before the coronagraph scaled by  $(1-S)$  where  $S$  is the Strehl ratio of the system up to the coronagraph spot. Since the pupil after the coronagraph is not uniformly illuminated, correcting for both pre- and post-coronagraph errors with the deformable mirror is similar to correcting intensity errors (ie, possible only with half-dark hole algorithms and in monochromatic light.) We have assumed that these errors cannot be corrected and placed a requirement on post-coronagraph optics as given in Table 1. These errors are currently assumed to be uniformly distributed in radius, which is a conservative assumption; Fourier simulations of the coronagraph can be used to evaluate their properties in detail.

Note that if the coronagraph is an apodizer (including shaped pupils) with no focal stop, then there are no “post-coronagraph” aberrations and all aberrations can be removed through image sharpening. However, even an apodized coronagraph may still include a focal stop to remove scattered light, in which case errors after that stop would be in this category. Phase errors in or after a nulling coronagraph are similarly uncorrectable.

The distribution of these errors between low, mid and high frequencies comes from a power law, currently set so that the power per unit spatial frequency  $k$  in is proportional to  $k^{-2.5}$ ; appropriate distributions should be studied in more detail. Within a given bin the errors are assumed to be flat, which is clearly incorrect and causes contrast at small angles to be overestimated and contrast at large angles to be underestimated. (See future documents on optical error distributions#?)

#### **4.8 Internal intensity errors**

As noted by Joe Green and collaborators at JPL, internal phase errors at planes not conjugate to the DM will result in mixed phase and intensity errors in the pupil plane; when the phase component of these errors are corrected the intensity component will remain. Numeric simulations are being carried out at LLNL to explore the magnitude of these effects – preliminary versions show that the mid-frequency component must be less than 10 nm RMS.

#### **4.9 Scintillation**

Work in progress; report from Marcos van Dam to be forwarded soon. Simulations indicate that for a median CN2 profile scintillation is not a dominant term in the error budget but for a worst-case (high jet stream) case it may be.

## Appendix: analytic techniques and PSF formalism

The figure of merit for the error budget of an ExAO system is not the total RMS wavefront error or Strehl ratio, but the final achievable contrast. This means that we require tools – analytic or simulation – for translating different wavefront error terms into their effects on contrast. Several families of simulations have been used to predict ExAOC performance, ranging from detailed wave-optics simulations to semi-analytic error budgets as given in this document. The full optics simulations (e.g. those of the SFWFS) can be used to determine the detailed behavior of system components, but are computationally prohibitive for determining final sensitivities. Simulating one second of exposure time at twice Nyquist sampling with our current codes takes ~16 hours on a dual-processor Macintosh G5, and many effects (such as small static wavefront errors) only become apparent in hour-long exposures. We use two techniques for predicting final sensitivity. The first are Monte Carlo Fourier-domain simulations in which a series of independent phase screens are generated to represent timesteps separated by the individual speckle lifetimes rather than the AO update rate. The AO correction is simulated with a Fourier-domain filter, and additional error sources such as measurement noise or temporal bandwidth are modeled as additive noise at appropriate spatial frequencies and shifts in the corrected phase. These techniques are being used to produce the sensitivity predictions used in the science case. However, even this technique is too computational intensive to explore a variety of system designs, so we must turn to semi-analytic error budgets.

As shown by Sivaramakrishnan et al.<sup>4</sup>, the high-contrast PSF in the high-Strehl regime can be written as the sum of a diffraction pattern term, a “pinned speckle” term which also traces the diffraction pattern, and a PSF halo term. The first two can be suppressed by a coronagraph. The third term, which dominates the wings ( $>3-5 \lambda/D$ ) of an ExAO system with an effective coronagraph, is essentially the power spectrum of the residual phase errors. This provides a natural way to predict the long-exposure average PSF and final sensitivity to pointlike companions. Assuming there are  $n$  distinct wavefront error sources  $\phi_i$  and all are uncorrelated, the total PSF

intensity (normalized to unity) is given by  $P(\theta) = \sum_i^n \sigma_i^2 I_i(\theta)$  where  $I_i(\theta) = \langle |\Phi_i(\theta/\lambda)|^2 \rangle / \sigma_i^2$  is a

the unity-normalized spatial power spectrum of the phase error  $\phi_i$  and  $\sigma_i$  is the magnitude of the corresponding phase error in radians. A phase error of spatial frequency  $\theta/\lambda$  in cycles per meter ( $D\theta/\lambda$  in cycles per pupil) will scatter light to an angular radius  $\theta$ . This leads to a useful insight: in order to detect planets at radii between 0.2 and 1 arcsecond at H band, we need to control phase errors between ~3 cycles per pupil and ~30 cycles per pupil. Lower frequency errors will primarily rearrange light under the coronagraph occulting stop (though the details of how light leaks through the coronagraph are complex for different designs) while higher frequencies scatter light to large radii. Reducing the errors at mid frequencies results in a PSF with a “dark hole”<sup>5</sup> or basin in which planets can be detected.

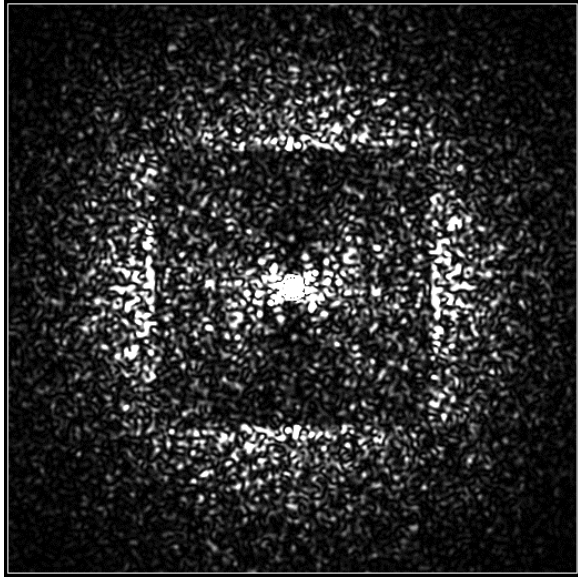


Figure 6: Instantaneous monochromatic PSF showing speckles

Instantaneously, the PSF is completely broken up into speckles (Figure 6)– and these speckles are the main source of noise in an attempt to detect a pointlike object such as a planet. The noise as a function of radius for a single PSF noise source in monochromatic light is given by  $\sigma_i^2 I_i(\theta)$  - the noise is roughly equal to the intensity. (In broadband light, an additional term appears decreasing the noise due to the elongation of the speckles; for clarity we will omit this term in this section, though it has been included in our error budget in section 4.) Over a long integration, multiple realizations of the speckle pattern will act to smooth the PSF. We express this by assigning each error source a characteristic speckle decorrelation timescale  $tdec_i$ ; in an integration time  $t \gg tdec_i$ , the final noise for a single

source will be given by  $s\sigma_i^2 I_i(\theta) \left(\frac{tdec_i}{t}\right)^{1/2}$  where  $s$

is a speckle noise scaling factor, evaluated through simulations to be  $\sim 0.25$ , similar to the value given by Racine et al (reference...).

If multiple error sources are present, Sivaramakrishnan et al (2002) show that each decorrelates independently, and the total noise in the final image is given by

$$N(\theta, t) = \sum_i^n \sigma_i^2 I_i(\theta) \left(\frac{tdec_i}{t}\right)^{1/2}$$

This means that error sources with rapid decorrelation, such as the random measurement noise of the AO system, are much less significant than errors that decorrelate slowly, such as the atmospheric fitting and bandwidth terms. Errors that do not decorrelate, such as quasi-static optical errors, are the worst of all; as shown by Sivaramakrishnan et al, in an extremely long exposure with both random and static errors, the PSF approaches the noise floor given by the static errors only – the PSF becomes a smooth halo with imprinted on it a speckle pattern equivalent to that given only by the static errors. Figure 3 illustrates this and shows the severe effect of even small static PSF errors.

<sup>1</sup> Racine, R., et al. 1999 PASP 111, 587

<sup>2</sup> Sparks, W.B and Ford, H.C 2002, ApJ, 578, 543

<sup>3</sup> Herriot, G., et al. 2004 Proc. SPIE 5490 (this volume)

<sup>4</sup> Sivaramakrishnan, A., Lloyd, J. P., Hodge, P. E., and Macintosh, B. A. 2002, ApJ, 581, L59

<sup>5</sup> Malbert, F., Yu, J. W., and Shao, M., 1995 PASP 107, 386